An airfoil-based synthetic actuator disk model for wind turbine aerodynamic and structural analysis

Muhammad Rubayat Bin Shahadat [a,b,1], Mohammad Hossein Doranehgard [a,b,1], Weibing Cai [a,c], Charles Meneveau [b], Benjamin Schafer [c], Zheng Li [a,*]

[a] Deptartment of Mechatronics Engineering, Morgan State University, Baltimore, MD, 21251, USA
[b] Deptartment of Mechanical Engineering, Johns Hopkins University, Baltimore, MD, 21218, USA
[c] Deptartment of Civil and Systems Engineering, Johns Hopkins University, Baltimore, MD, 21218, USA

ARTICLE INFO

ABSTRACT

This study introduces an airfoil-based refinement technique to enhance the Actuator Disk Model (ADM) for improved wind turbine aerodynamic load prediction and structural simulation in conjunction with Large Eddy Simulations of the wind flow. While ADM offers higher computational efficiency than the more detailed but resource-intensive Actuator Line Model (ALM), it traditionally lacks the resolution needed to capture the localized blade forces accurately. To address this limitation, we introduce a refinement technique that uses airfoil-specific data and employs interpolation-based grid point refinement, achieving ALM-comparable accuracy while preserving ADM's efficiency. Unlike conventional ADM that provides only rotor-disk averaged forces, our synthetic method tracks transient aerodynamic load variations over multiple blade revolutions, allowing us to calculate the distributions of maximum and minimum loads during typical cycles. Applied to the NREL 5 MW reference turbine, our enhanced ADM accurately predicts key aerodynamic parameters (angle of attack, axial velocity, lift, drag, axial and tangential forces along the blades) as well as structural responses (blade tip deflection, maximum stress, and stress concentration). Our results show that the tip deflection ranges from 2.33m (3.69 % of blade length) to 4.28m (6.79 %), with maximum stress concentration occurring near the blade root. This research demonstrates that a refined synthetic ADM approach can serve as a computationally efficient alternative for both aerodynamic analysis and structural simulation of wind turbine blades subjected to realistic wind fields.

1. Introduction

1.1. Background

Wind energy represents a cornerstone of sustainable power generation, offering a renewable and efficient solution to tackle the challenges of climate change and energy security [1]. Modern wind technology has evolved dramatically, with turbine capacities expanding from hundreds of kilowatts to multi-megawatt systems exceeding 15 MW for offshore applications, dramatically improving cost-effectiveness and energy capture [2]. As a naturally replenishing resource with minimal carbon footprint during operation, wind power has emerged as one of the most economically viable alternatives to fossil fuels, with global capacity expanding exponentially over the past decade [3]. This remarkable growth trajectory is evidenced by wind energy's unprecedented installation rates across both developed and emerging economies, with China, the United States, and European nations leading substantial capacity additions that are transforming their energy landscapes [4]. The versatility of this technology enables deployment across diverse geographical contexts-from offshore installations harnessing powerful marine winds to distributed small-scale turbines serving remote communities. Beyond environmental benefits, wind energy contributes significantly to economic development through job creation, reduced energy import dependence, and price stability unaffected by fuel market volatilities [5, 6]. As energy systems worldwide undergo transformation toward greater sustainability, the continued advancement and integration of wind energy represent critical components in achieving both national energy policies and international climate commitments [7].

* Corresponding author.
   E-mail address: zheng.li@morgan.edu (Z. Li).
[1] The authors contributed equally to this work.

Accurately determining wind forces acting on turbine blades is essential for enhancing efficiency and maintaining structural durability. These forces depend critically upon the inflow wind fields characterized by turbulent flow structures and variability occurring at multiple spatial and temporal scales. Large Eddy Simulations (LES) of wind fields can capture much of this variability in a realistic fashion [8]. Among the computational approaches employed to represent the wind turbines in LES, the Actuator Disk Model and Actuator Line Model stand out as significant methodologies [9]. These techniques simulate wind-blade interactions with varying degrees of sophistication and computational demands, providing engineers with critical insights into turbine aerodynamics. The ADM represents turbine rotors as a permeable disk applying spatially uniform force across the rotor disk area. Its computational efficiency and straightforward implementation make it ideal for extensive simulations where precise blade geometry is less important [10,11]. This approach works particularly well when analyzing general wake patterns and flow fields rather than specific blade-level phenomena [12]. A limitation of ADM is that it does not provide detailed information about blade loading at various positions along the blade [13].

Conversely, ALM depicts blades as segmented force vectors arranged along the blade length. This approach delivers a more detailed aerodynamic representation, successfully reproducing sophisticated flow features including root and tip vortices [13,14]. ALM is a proven technique especially when precise prediction of blade loading is required, such as during irregular inflow conditions or aeroelastic investigations [14]. Its capability to accurately model more detailed force distributions makes it a preferred methodology for researchers conducting detailed blade-level simulation studies [15].

This study introduces an interpolation-based refinement technique designed to improve the resolution of the ADM, enabling it to produce predictions for both aerodynamic parameters (angle of attack, axial velocity, drag, lift, axial and tangential forces) and structural parameters (tip deflection, and maximum stress concentration) that closely align with those of the more detailed ALM while preserving its computational efficiency. By enhancing ADM's accuracy, this synthetic approach allows for a better representation of aerodynamic forces acting on the composite blades of wind turbine without significantly increasing computational costs.

While simulating the structural behavior of wind turbines using the load data from our airfoil-based synthetic ADM approach, it is important to note that composite blades, being highly flexible, are among the most critical components of the wind farm. These blades endure complex loading conditions, including aerodynamic forces, gravity, and centrifugal forces, making accurate modeling essential for reliable performance predictions [16]. Therefore, understanding the underlying mechanism of the deformation and blade failure is vital to optimize structural design and enhance long-term durability [17]. As an alternative to analytical solutions and experimental observations, Finite Element Analysis (FEA), due to its convenience and rapidity, has been widely used to analyze the eigenfrequencies and tip deflections of blades, and predict their deformation and stress-strain distribution with good accuracy. Larsen et al. [18] utilized an nonlinear structural solvers to study the effects of blade tip deflection on its stability, and simulated results reveal that large blade deflections can change the effective rotor area, thereby altering the blade and turbine loading. In addition, a numerical model proposed by Mazarbhuiya et al. [19] employed to analyze the effect of blade thickness on the power coefficient and tip speed ratio at low wind speed, and their work found that the wind speed determines the selection of blade thickness. More specifically, we prefer to select a thicker blade when the low wind speed conditions emerge. Subsequently, nonlinear modeling is proposed to analyze the effect of material strength on blade deformation [20]. The results suggest that the increment of the blade strength can remarkably improve blade performance and optimize blade selection. In practice, the wind blades would experience damage and delamination failure under extreme loading, which would reduce the load-carrying capacity of the laminates. Therefore,

some researchers turn to the investigation on delamination damage and failure induced by pre-existing defects and degradation. The effects of various wind velocities on damage evolution of the blade skin, shear web and adhesive layer are investigated by Liu et al. [21]. Moreover, a wind blade with the length of 52.3 m is established by Chen et al. [22], and their simulated results reveal that the delamination between spar cap and shear web yields the blade collapse. The full-scale test of turbine blade with the length of 34 m is conducted to investigate crack initiation and propagation of trailing edge, and the effect of bulking on trailing edge failure is highlighted [23]. Recently, Li et al. [21] proposed a new method to predict the damage process of blade spar cap, and the local material degradation induced by pre-existing defects is also studied. Such results suggest that the delamination evolves from intralaminar to interlaminar, thereby transforming the local failure into global failure. However, the existing research on the delamination of wind turbine blades mainly focuses on damage and failure of blade under static load, and the effect of transient wind force on the blade performance remains unanswered. More specifically, how to accurately apply the wind force on the blade is challenging, since it varies along blade length and loading times.

1.2. Novelty and research gap

The novelties and contributions of this work can be summarized as follows.

- ADM offers computational efficiency but lacks resolution in capturing localized blade forces, while ALM provides higher accuracy at a greater computational expense. Few studies have attempted to bridge this gap by enhancing ADM's resolution while preserving its efficiency.
- To our best knowledge, no previous research has analyzed the transient variation of aerodynamic loads during turbine blade revolutions using ADM. Existing ADM studies typically report time-averaged force values, leaving the detailed time-dependent evolution of loads across multiple revolutions unexplored. Our research introduces a novel approach to track maximum and minimum force variations over consecutive blade revolutions.
- Although some studies have examined transient aerodynamic loads in wind turbines, most research continues to emphasize time-averaged load distributions for structural simulations. Limited research exists using ADM to study transient aerodynamic force variations across multiple blade revolutions. We develop a refined ADM approach that interpolates load data to achieve ALM-comparable accuracy, enabling realistic structural simulations at a reduced computational cost.

2. Numerical details

In this study, we have employed a LES code combined with the Lagrangian scale-dependent dynamic method [24] to model turbulence in the atmospheric boundary layer. Although detailed documentation of the computational methodology can be found in previous publications [24–27], our analysis specifically focused on two major components: the framework for atmospheric simulation (discussed in subsection 2.1) and the wind turbine representation (covered in subsection 2.2).

2.1. Atmospheric boundary layer (ABL) modeling

The numerical simulation utilizes a LES algorithm that solves the incompressible and filtered N-S equations in a neutrally stratified atmosphere driven by pressure gradient forcing [28]:

$$\partial_i u_i = 0 \tag{1}$$

$$\partial_t u_i + u_j \left(\partial_j u_i - \partial_i u_j \right) = - \partial_i \left(\frac{p^*}{\rho} \right) + \vartheta \partial_j \partial_j u_i + f_i - \partial_j \tau_{ij}^d - \partial_1 \left(\frac{p_\infty}{\rho} \right) \delta_{i1} \tag{2}$$

where, p^*, u_i, and p denote, respectively, the modified pressure term, the filtered velocity component, and the real pressure. Also, $1/3 \; \tau_{kk}$ (the trace of the subgrid-scale stress tensor), $1/2 \; \rho u_i u_i$ (kinetic energy), and $\tau_{ij}^d = -2 \left(c_s \Delta \right)^2 |S| S_{ij}$ (the deviatoric component of the subgrid-scale stress tensor) [24] are appeared in Equation (2). Viscous influences are considered insignificant within this formulation due to the flow's high Reynolds number characteristics. $\frac{dp_\infty}{dx}$ (mean pressure gradient) is imposed to maintain the flow consistency.

The bottom boundary condition employs an aerodynamic surface roughness parameter of $z_0 = 5 \times 10^{-4} H$, which corresponds to 0.5 m. The influence of wind turbines is modeled via a resistive drag force (denoted in the term f_i) that counteracts the pressure-gradient-driven flow. In Equations (1) and (2), repeated indices follow the Einstein summation convention, with the pressure gradient forcing operating exclusively along x_1 (the streamwise axis). It should be mentioned that the velocity components and coordinate system are expressed as: wall-normal (w, z), spanwise (v, y), and streamwise (u, x).

The simulation domain implements periodic boundary conditions along both horizontal axes (x and y). The computational region rises 1000 m in height (H) and spans roughly 3142 m across both horizontal dimensions (L). Numerical resolution is achieved through a grid structure comprising $192 \times 192 \times 97$ points, with horizontal grid spacing of $\Delta x = \Delta y = 16.4$ m and vertical spacing of $\Delta z = 10.4$ m. The Kolmogorov length scale (η) at the hub height is estimated to be approximately 1 mm, and the ratios of the grid spacings to the Kolmogorov scale are $\Delta/\eta \approx 16400$ (x/y) and ≈ 10300 (z). These values confirm that the mesh lies well within the LES regime, where energy-containing eddies are resolved and small-scale dissipation is modeled through the subgrid-scale formulation.

The entirety of LES simulations maintains uniform dimensional boundary layer height (H), and pressure gradient ($\frac{dp_\infty}{dx}$), although actual atmospheric boundary layers would naturally modify their vertical extent in response to the roughness of the lower boundary. The effective surface roughness is being altered by the presence of the wind turbines [26]. Also, computational limitations prevent dynamic adjustment of domain height, and roughness variations influence the bulk flow velocity in relation to the velocity scale $u_p = \sqrt{\frac{dp_\infty}{dx} \frac{H}{\rho}}$. To compensate for these differences, results at the domain's upper boundary will be typically normalized by the mean velocity at the top of the domain (U). While an alternative strategy could involve implementing adjustable pressure gradients to ensure consistent mean velocities across different simulations, the post-processing normalization technique delivers comparable outcomes with significantly reduced complexity.

To perform the simulation, we have used LESGO (https://lesgo.me.jhu.edu/) which is an open source computational fluid dynamics (CFD) solver developed by the Turbulence Research Group at Johns Hopkins University (JHU) for simulating turbulent flows, particularly in atmospheric boundary layers and wind farm environments. It employs a pseudo-spectral method in two spatial directions, while the third direction is handled using a finite-difference approach. This hybrid scheme allows for efficient calculations with high numerical accuracy, making it well-suited for large-scale turbulence simulations. Time evolution of the governing equations is handled using the Adams-Bashforth scheme, which provides a balance between accuracy and computational efficiency. To model small-scale turbulence, LESGO incorporates subgrid-scale (SGS) models, including the standard Smagorinsky model with a fixed coefficient and a scale-dependent dynamic model. These models help represent the effects of unresolved turbulence, which are crucial in different types of flows. A key numerical consideration in LESGO is the resolution balance between spectral and finite-difference directions. Since spectral methods resolve turbulence more efficiently

than finite-difference approaches, an optimized resolution ratio is necessary to ensure consistency in turbulence statistics. Through numerical analysis, it has been found that using a finer resolution in the finite-difference direction compared to the spectral directions improves the accuracy of Reynolds stress predictions [29].

2.2. Turbine modeling

In this study, we have simulated a single wind turbine using the Actuator Disk Model and compared its results with a high-fidelity Actuator Line Model approach from the literature. Numerical modeling plays a critical role in understanding wind turbine aerodynamics, and both ADM and ALM provide valuable insights at different levels of accuracy and computational cost [29–31]. As we have already discussed, the ADM simplifies turbines as stationary disks, offering efficiency for large-scale wake studies but lacks blade-level detail. In contrast, the ALM captures detailed blade aerodynamics and wake dynamics, though at a much higher computational cost [30,31].

In the actuator disk model (ADM), each turbine's interaction with the flow is represented by a spatially distributed thrust force, defined as [30]:

$$F_x = -\frac{1}{2} C_T' \rho \left(u_d^T \right)^2 A_T \tag{3}$$

The thrust coefficient C_T' is defined with respect to the disk velocity, rather than traditional formulations based on upstream velocity [30]. The quantity u_d^T denotes the velocity averaged across the rotor disk, which is temporally filtered using a first-order exponential smoothing function. A_T is the rotor's total swept area. To ensure numerical stability, particularly within the pseudo-spectral solver, a Gaussian-filtered indicator function is employed to smoothly distribute the thrust force across the computational grid. The instantaneous power extracted by the turbine is computed as the product of the applied thrust force and the filtered disk-averaged velocity [30]:

$$P = F_x u_d^T = -\frac{1}{2} C_T' \rho \left(u_d^T \right)^3 A_T \tag{4}$$

Additional details on the implementation methodology of the actuator disk model can be found in prior studies [29–31].

In this study, we first simulate a single turbine using ADM, capturing its wake characteristics and flow interactions. Then, we incorporate airfoil data to compute aerodynamic loads, allowing a direct comparison between ADM and prior ALM predictions available in the literature for the same turbine. This comparison helps assess the trade-offs between computational efficiency and accuracy in predicting aerodynamic load and structural response. The results provide insights into optimizing wind turbine modeling approaches for both standalone turbines and larger wind farm simulations.

2.3. Simulation setup

2.3.1. Wind turbine simulation

The computational domain used in this study is designed to accurately capture the dynamics of wind turbine wake interactions while ensuring sufficient spatial resolution. The domain dimensions are 24D × 8D × 24D in the streamwise (x), vertical (z), and spanwise (y) directions, respectively, where D represents the rotor diameter (Fig. 1(a)). The turbine, representing as the actuator disk, is positioned at 4D downstream from the inlet boundary and centered laterally within the domain. The wake length has been calculated (will be discussed later) and the downstream length of 20D is long enough to avoid any wake effects.

The computational domain consists of $192 \times 192 \times 97$ grid points in the streamwise, spanwise, and vertical directions, ensuring adequate resolution for resolving turbulence structures while maintaining computational efficiency. The detailed grid resolution study can be
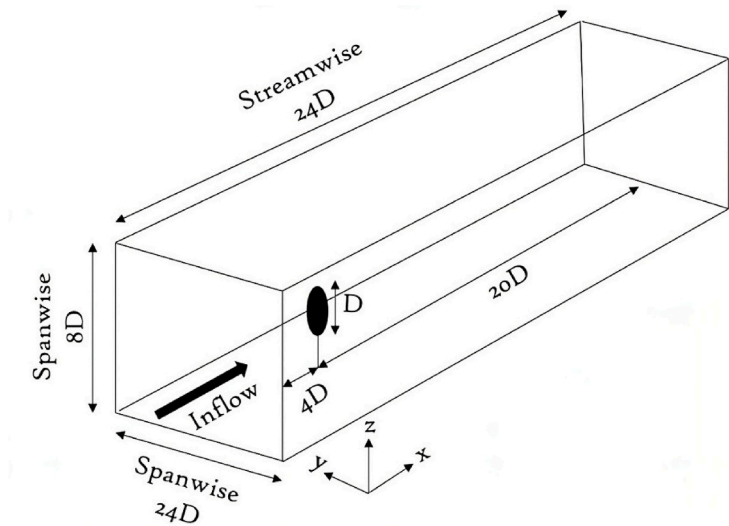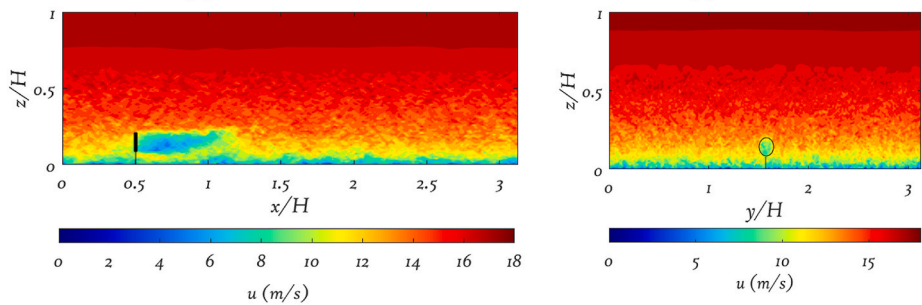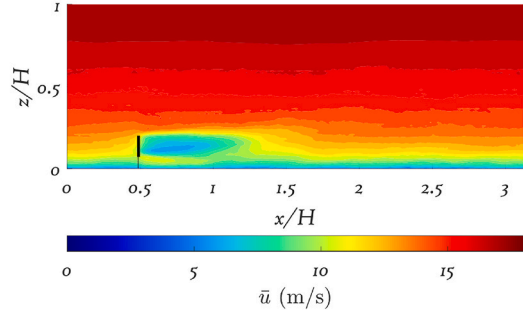
(a)
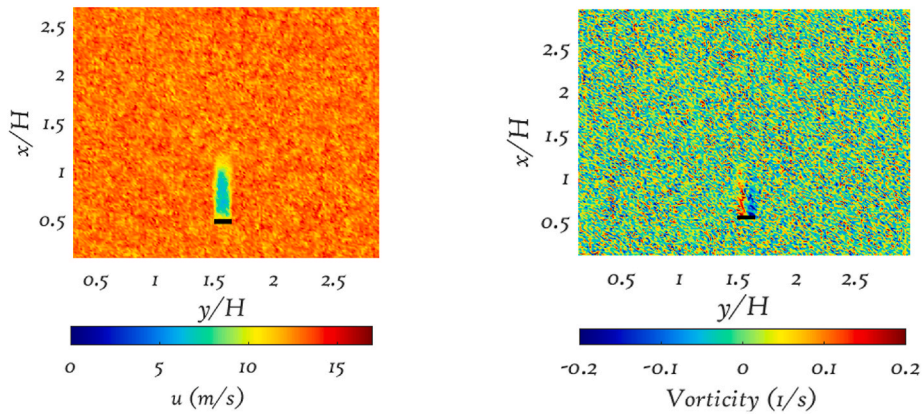
(b)

(c)

(d)

(e)

(f)

(caption on next page)

4

Fig. 1. Various aspects of the computational domain and wake characteristics in the simulation. (a) schematic of the computational domain, highlighting the turbine location and domain dimensions in the streamwise, spanwise, and vertical directions. (b) the instantaneous streamwise velocity field in the *x-y* plane, where a distinct low-velocity region forms behind the turbine due to wake effects. (c) corresponding vorticity field, revealing the shear layers and turbulence structures generated by the wake. (d) the instantaneous streamwise velocity field in the *x-z* plane, capturing the vertical development of the wake and its interaction with the atmospheric boundary layer. (e) the instantaneous streamwise velocity field in the *y-z* plane (f) the time-averaged streamwise velocity field, providing a clearer view of the wake deficit and its gradual recovery due to turbulence mixing. The domains in these figures are zoomed for a better visualization.

found in our previous literature [30]. A uniform grid spacing is used in all the horizontal directions (x, y), with a smaller grid spacing applied in the vertical (z) direction to better capture the boundary layer effects. A fully developed atmospheric turbulent boundary layer is imposed at the inlet without the use of a precursor run. Turbulence is generated internally by the interaction of the flow with the rough bottom surface and the imposed pressure gradient, following the well-established approach for ABL simulations. As we have already mentioned, a streamwise mean pressure gradient is applied to drive the flow, and periodic boundary conditions are implemented in both horizontal directions. The bottom boundary utilizes an equilibrium wall stress model with a roughness length of $z_0 = 5 \times 10^{-4} H$. This setup allows the flow to naturally evolve into a turbulent boundary layer over time, ensuring realistic inflow turbulence characteristics.

The wake characteristics of the actuator disk model are analyzed using velocity and vorticity fields (Fig. 1(b) and (c)). The instantaneous streamwise velocity field (Fig. 1(b)) shows the velocity distribution in the x-y plane, where the wake of the turbine is clearly visible as a low-velocity region extending downstream. The gradual increase in velocity further downstream indicates wake recovery due to turbulent mixing. Meanwhile, the vorticity field (Fig. 1(c)) highlights the presence of coherent vortex structures generated by the wind turbine wake. The vorticity contours reveal the shear layers between the high-speed inflow and the low-speed wake, where turbulence intensifies as coherent structures break down into smaller eddies [31]. At hub height, we estimate the streamwise turbulence intensity of approximately 15 % as the ratio of the root mean square of streamwise velocity fluctuations to the mean streamwise velocity. We also estimate the integral length scale of approximately 1.8D using spatial autocorrelation [32]. These properties are not prescribed at the inlet but arise naturally through the flow physics, making the current approach well-suited for investigating wind turbine behavior in realistic boundary layer conditions. To further analyze the wake structure, Fig. 1(d) presents the instantaneous velocity field in the x-z plane, capturing the wake evolution in the vertical direction. The figure demonstrates a distinct low-velocity region downstream of the turbine, where the wake is influenced by the turbulence in the atmospheric boundary layer. The interface between the wake and the outer flow is characterized by strong shear, leading to turbulence generation and wake recovery at further downstream distances. Additionally, Fig. 1(f) illustrates the time-averaged streamwise velocity field, which provides a clearer picture of the wake structure by filtering out instantaneous fluctuations. The wake deficit is most prominent near the turbine, and as the flow progresses downstream, wake recovery becomes evident due to turbulent mixing. The average wake length estimated based on the time-averaged velocity fields is approximately 10D. From the time average velocity profile, it is observed that the region of significant velocity deficit persists until approximately $x/H = 1.7$. The wake length estimation was based on the recovery of streamwise velocity to freestream values in the velocity field. Since the length of the wake is approximately 10D, we have extended the domain up to 20D after the turbine to avoid any wake effect. Fig. 1(e) shows the instantaneous streamwise velocity on a cross-sectional plane at the location of the turbine $x/H = 0.5$. The circular region represents the turbine disk area. A localized velocity deficit is observed within this area, consistent with the expected turbine-induced momentum extraction. Outside the rotor area, the streamwise velocity returns to freestream conditions.

2.3.2. Structural simulation

The wind turbine blade used in this study corresponds to the NREL 5 MW reference turbine and is discretized into shell elements for structural analysis (Fig. 2(a)–(c)). The blade was designed by the National Renewable Energy Laboratory (NREL) and has a rotor diameter of 126m and height of 90m [33]. The blade consists of aerodynamic skins and shear webs, which provide structural integrity and stiffness to withstand aerodynamic and gravitational forces. The blade root is fixed, while lift and drag forces act on the blade, with lift directed along the y-axis and drag along the -z axis.

The blade skin follows a sandwich composite structure comprising three distinct material layers (Fig. 2(d)). The outer layers consist of carbon-epoxy laminate (2.8 mm thick) and glass-vinyl ester laminate (11.2 mm thick), while the core is composed of PVC foam (150 mm thick). The fiber orientations within the glass-vinyl ester laminate are optimized for structural performance, incorporating 0°, −45°, 45°, and 90° fiber angles, with each layer having a thickness of 1.4 mm. This layered arrangement enhances the blade's ability to withstand torsion, compression, and shear forces under operational conditions [33–35].

The detailed material properties, structural characteristics and aerodynamic properties of the NREL 5 MW wind turbine blade are summarized in Tables 1 and 2. The carbon-epoxy and glass-vinyl ester laminates are modeled as transversely isotropic materials, ensuring realistic structural responses under aerodynamic loading [36]. Along the blade span, there are varying DUxx and NACA 64 airfoils. In this study, delamination failure is not considered, as the primary focus is on the aerodynamic loads and structural response under normal operating conditions.

3. Determining aerodynamic load using airfoil data

The Actuator Disk Model is commonly used in large-scale wind farm simulations due to its computational efficiency. However, a key limitation of ADM is its uniform force distribution, which does not represent the actual aerodynamic loading on the turbine blades. This uniform forcing neglects spanwise variations in chord length, twist angle, angle of attack, and resulting aerodynamic forces-factors that significantly influence turbine loading under realistic flow conditions. To improve the accuracy of ADM while maintaining computational feasibility, we have assumed a line passing through the flow field instead of an actuator disk. Then we introduced an interpolation-based refinement strategy that increases the number of grid points along that line. This interpolated grid enhances spatial resolution and enables the incorporation of airfoil-based aerodynamic forces. Instead of applying uniform thrust, we compute lift and drag forces at each interpolated point using local flow conditions and airfoil-specific characteristics, such as pitch angle and angle of attack. The lift and drag coefficients are retrieved from airfoil data tables based on the NREL 5 MW turbine design. These forces are then resolved into normal and tangential components. This modification allows for a more physically representative force distribution, while remaining significantly less computationally expensive than actuator line or blade-resolved models. The details of the airfoil data implementation, along with a step-by-step description and flowchart (Fig. 3), are provided in the following part of this section.

As we have already mentioned, the actuator disk model requires low resolution around the turbine disk whereas the actuator line model requires very high resolution along the blades. In our simulation, we have around 8 grid points in y direction and around 12 grid points in the z
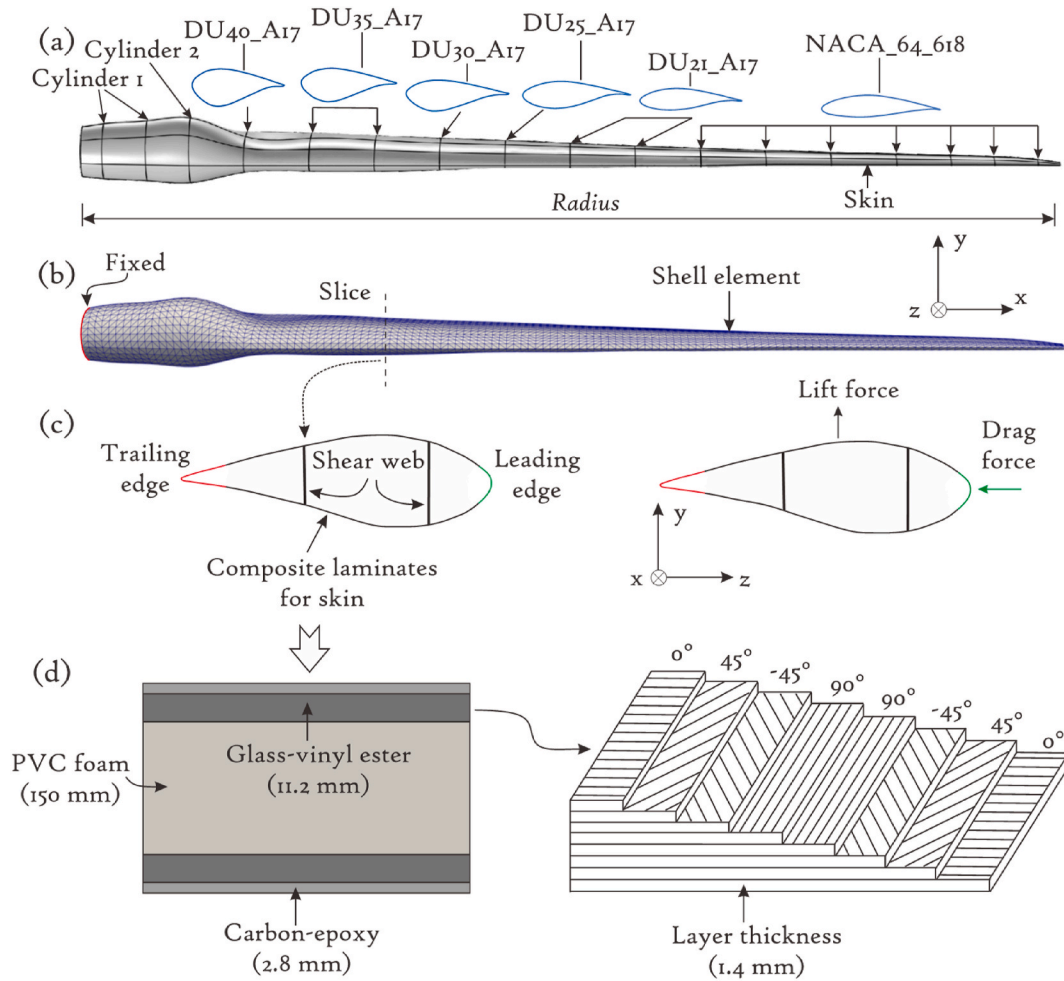
Fig. 2. (a) Geometry of the NREL 5 MW wind turbine blade with different airfoils along the radius. (b) Finite element mesh representation of the blade indicating the fixed end. (c) Cross-sectional view of the blade, illustrating the shear web, aerodynamic forces, and composite laminates. (d) Sandwich structure of the blade skin, showing the layered materials and fiber orientation within the glass-vinyl ester laminate [33–36].

Table 1
Input parameters for composite materials [36].

Input parameters	Carbon-epoxy	Glass-vinyl ester	PVC foam
E_1 (GPa)	139	41	0.25
E_2 (GPa)	9	9	0.25
E_3 (GPa)	9	9	0.25
Shear modulus G (GPa)	5.5	4.1	0.0926
Bulk density, ρ (kg/m^3)	1560	1890	200
Poisson's ratio, ν	0.32	0.3	0.35

*Note that E_1, E_2 and E_3 are Young's modulus in the x, y and z directions respectively.

Table 2
The blade sections and airfoils of NREL 5 MW wind turbine blade [33,37].

Node	Position (m)	Chord (m)	Twist (°)	Airfoil
1	2.87	3.542	13.308	Cylinder 1
2	5.6	3.854	13.308	Cylinder 1
3	8.33	4.167	13.308	Cylinder 2
4	11.75	4.557	13.308	DU40_A17
5	15.85	4.652	11.48	DU35_A17
6	19.95	4.458	10.162	DU35_A17
7	24.05	4.249	9.011	DU30_A17
8	28.15	4.007	7.795	DU25_A17
9	32.25	3.748	6.544	DU21_A17
10	36.35	3.502	5.361	DU21_A17
11	40.45	3.256	4.188	NACA_64_618
12	44.55	3.01	3.125	NACA_64_618
13	48.65	2.764	2.319	NACA_64_618
14	52.75	2.518	1.526	NACA_64_618
15	56.17	2.313	0.863	NACA_64_618
16	58.9	2.086	0.37	NACA_64_618
17	61.63	1.419	0.106	NACA_64_618

direction on the actuator disk. To mimic the actuator line in ADM setup, we have considered a line passing through the flow field. Since this line has low resolution, we have performed bi-linear interpolation to increase the number of grid points. Therefore, in the interpolated grid setup, this line has around 200 grid points. In this method, we are not resolving the actual blade, rather we use this line to construct a 3D representation of the blade using the airfoil data. Fig. 4(a) shows the instantaneous streamwise velocity field in the y-z plane at the location of the turbine x/H = 0.5, and 4(b) shows the zoomed view of the turbine in the flow field. Fig. 4(c)–(d) show the original grids and interpolated grids on the turbine blade, respectively. Fig. 4(e) shows the 3D view of the NREL 5 MW wind turbine blade showing different cross-sections and airfoil types.

Since the actuator disk is simulated without rotation, to mimic the real-world scenario and calculate the rotational velocity we have prescribed a certain angular velocity (ω). The velocity triangle at each radial position provides the relative velocity (U_{rel}) computed as [38,39]:

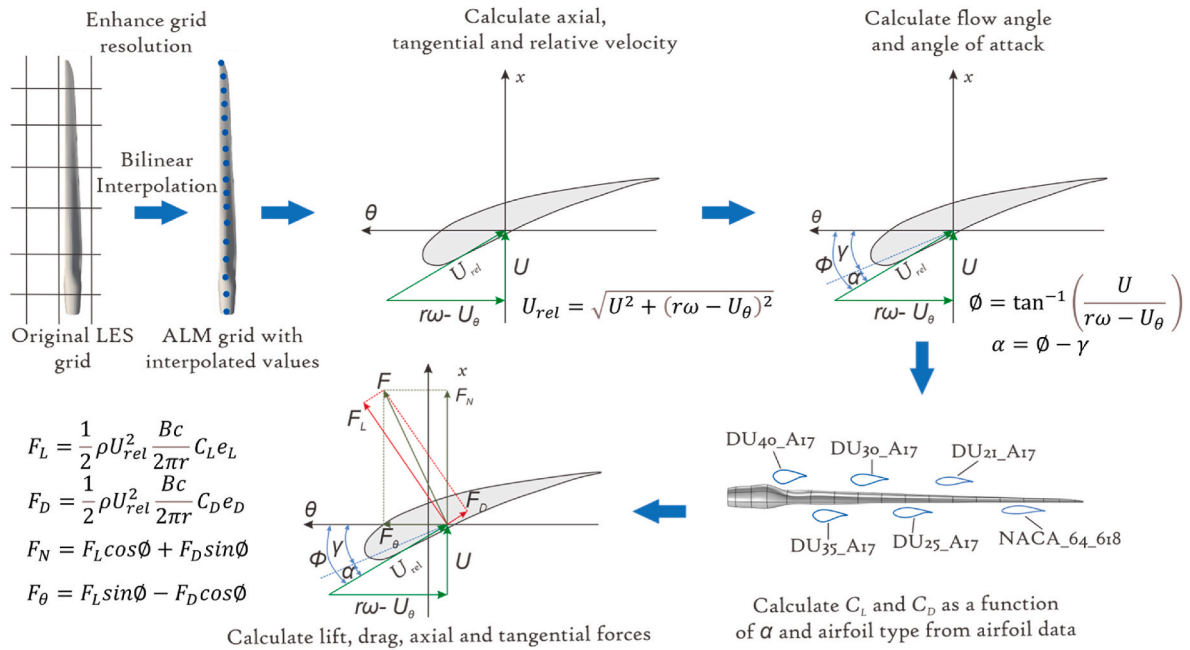$$U_{rel} = \sqrt{U^2 + (r\omega - U_\theta)^2} \tag{5}$$

Fig. 3. Step-by-step process for applying airfoil data in the actuator disk model, from interpolation and velocity calculations to determining lift, drag, axial and tangential forces [38,40]. The blade, airfoil and grid points are not properly scaled in this figure.
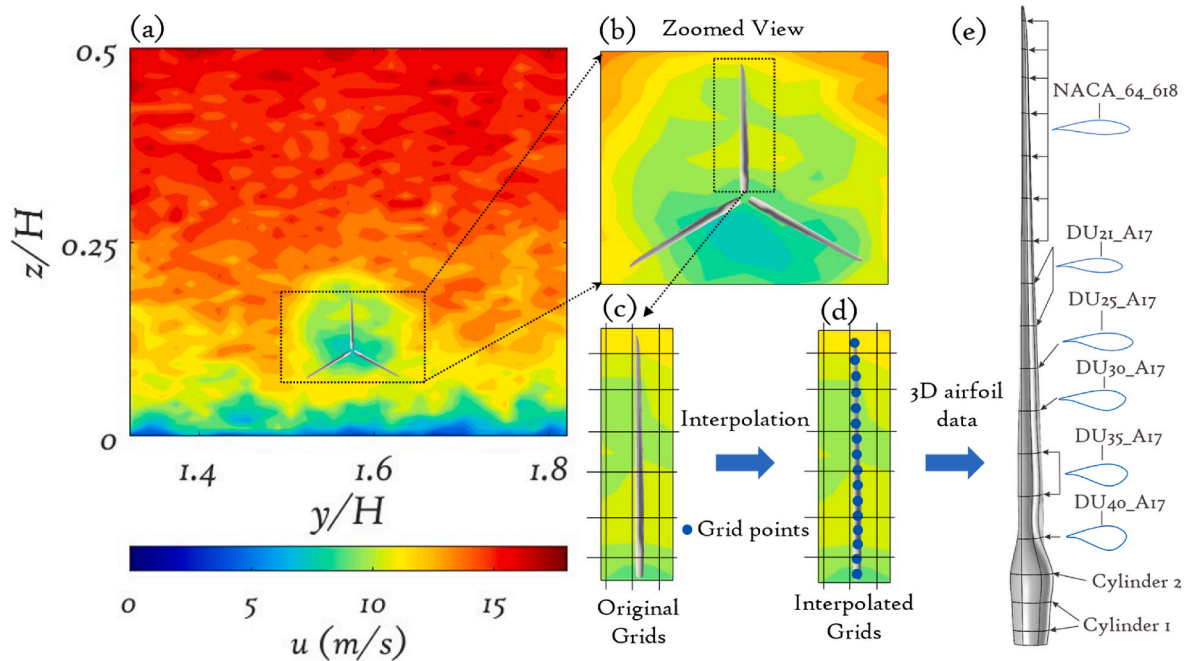

Fig. 4. (a) Instantaneous streamwise velocity field in the *y-z* plane at the location of the turbine *x/H* = 0.5. (b) Zoomed view of the turbine in the flow field (c) Zoomed view of a single blade in the original grids (d) Zoomed view of a single blade in the interpolated grids (e) 3D view of the NREL 5 MW wind turbine blade showing different cross-sections and airfoil type. The blade and the grid points are not properly scaled in this figure.

Where, U and U_θ are the axial and tangential velocity components of the air, ω is the rotor angular velocity and r is the local radial position along the blade.

Once we have the axial and tangential velocity components at the interpolated grids, we can calculate the local flow angle ($\emptyset$). The flow angle, determining the inclination of the relative velocity with respect to the rotor plane, is given by Refs. [38,39]:

$$\emptyset = \tan^{-1}\left(\frac{U}{r\omega - U_\theta}\right) \tag{6}$$

The local angle of attack (α) is computed as: $\alpha = \emptyset - \gamma$, where γ is the local pitch angle, determined by the twist distribution along the blade (Fig. 5) and any applied pitch adjustments. The incorporation of airfoil data begins at the calculation of the local angle of attack (α). Prior to this step, quantities such as the relative velocity and flow angle ($\emptyset$) are calculated without requiring airfoil-specific inputs. However, to
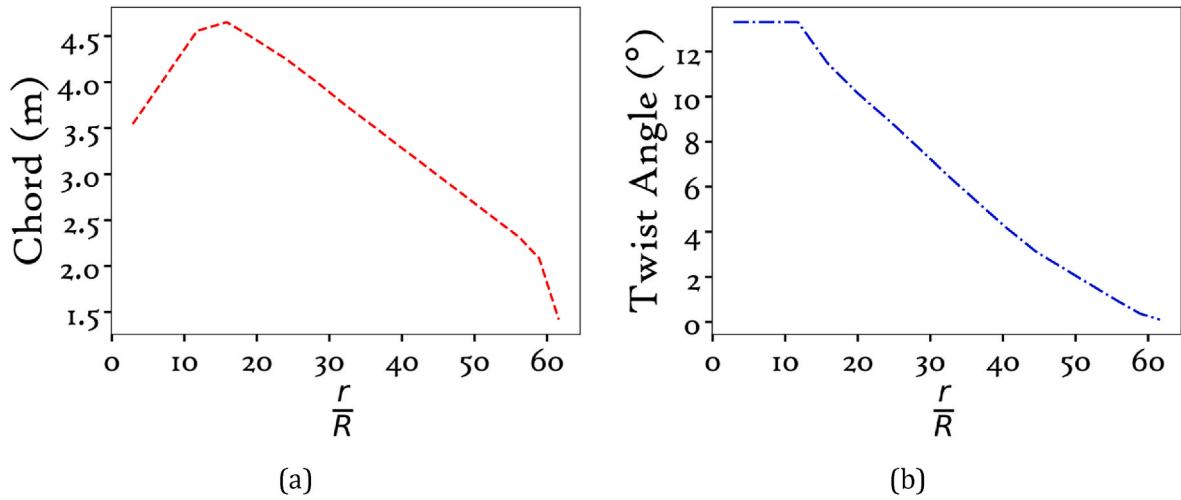
Fig. 5. (a) Chord length distribution (b) Twist angle distribution along the blade span for NREL 5 MW wind turbine.

compute local angle of attack (α), we introduce geometric blade information by subtracting the local pitch angle (γ), which is obtained from the twist distribution of the NREL 5 MW reference turbine. Once the angle of attack is determined, we retrieve the corresponding lift (C_L) and drag (C_D) coefficients from tabulated airfoil data at each radial location. These coefficients are functions of angle of attack (α), and are specific to the blade section's airfoil type. Using the angle of attack, the local lift (F_L) and drag (F_D) forces per unit area are computed as [38,39]:

$$F_L = \frac{1}{2}\rho U_{rel}^2 \frac{Bc}{2\pi r}C_L e_L \qquad (7)$$

$$F_D = \frac{1}{2}\rho U_{rel}^2 \frac{Bc}{2\pi r}C_D e_D \qquad (8)$$

Where ρ is the air density, c is the local chord length, B is the number of blades, C_L and C_D are the lift and drag coefficients, respectively which depend on the angle of attack. The local lift and drag coefficients are computed from the NREL 5 MW data table for each specific airfoil. Normally, tip and root corrections are multiplied with lift and drag forces. For simplification, we have not considered any tip or root corrections in this study. Finally, the local normal (F_N) and tangential (F_θ) components per unit area are obtained as [38,39]:

$$F_N = F_L cos\varnothing + F_D\ sin\varnothing \qquad (9)$$

$$F_\theta = F_L\ sin\varnothing - F_D\ cos\varnothing \qquad (10)$$

This airfoil-based actuator disk model offers a more physically realistic representation of wind turbine aerodynamics while preserving the efficiency of ADM. Although it does not resolve full blade geometry, it enables airfoil-informed loading distributions to be captured effectively. For better understanding, a flow chart illustrating the step-by-step implementation of this method has been shown at Fig. 3. After calculating all these parameters following the described method, we will compare our results with ALM from the literature in the next section.

4. Results and discussions

4.1. Comparisons to actuator line model

The performance of the synthetic Actuator Disk Model with airfoil data was assessed by comparing its results with the Actuator Line Model from the literature [29,38,39], focusing on angle of attack, aerodynamic load distribution, and velocity profiles along the blades. Given that a prescribed angular velocity is used, the blades are assumed to begin their rotation at $t = 0$ and complete a full cycle at $t = T$. For convenience, we

assume that at $t = 0$, the blade is positioned at the top of the rotor disk. However, this choice is arbitrary, as any location on the disk could be selected as the reference starting position for the blade's revolution. The primary objective of this study is to calculate the transient aerodynamic loadings at different blade positions during complete revolutions, compare them against ALM results from the literature, and utilize these load distributions for structural simulations. The profiles (Fig. 6) compared with ALM in this section are extracted from the blade position at $t = 0$ over multiple rotational cycles. These profiles feature three key representations: the average line, which denotes the mean values across multiple cycles, and the maximum and minimum variation lines, which illustrate the range of fluctuations observed within these cycles. This comparison serves to evaluate the accuracy of ADM in predicting aerodynamic forces while maintaining computational efficiency. It is important to acknowledge that the comparison between ADM with airfoil data and ALM from the literature is not perfectly exact due to differences in inflow conditions [29,38]. In our current LES, an atmospheric boundary layer is used as the inflow, whereas the ALM results from the literature were obtained under uniform inflow conditions [29]. As a result, rather than focusing on a direct numerical comparison, we emphasize the trends and overall magnitudes of the different parameters to assess the consistency between the models.

Fig. 6(a) represents the radial variation of the angle of attack (α) along the blade span. The ADM-predicted values show a strong agreement with ALM results. One interesting observation is that the angle of attack variation along the blade span using ALM always falls in between our maximum and minimum variation lines. The slight variations between ADM and ALM suggest that unsteady flow conditions introduce local deviations, yet the overall trend remains consistent with ALM predictions. A slight discrepancy in the trend is observed near the blade tip region ($r/R > 0.8$), which can be attributed to the absence of a tip correction factor in ADM. The average angle of attack variation from ALM in this region is less than $1°$. Since ADM assumes a force distribution without accounting for the blade effects at the tip, the trend of angle of attack near the tip is slightly different compared to ALM. Now, the variation of angle of attack is more pronounced in the mid-span region ($0.20 < r/R < 0.80$), where the maximum deviation from the ALM reference reaches approximately $3.5°$. This behavior is primarily attributed to stronger flow curvature and local velocity gradients in the mid-span region, which are more sensitive to modeling assumptions.

The aerodynamic forces, including drag force and lift force, are compared in Fig. 6(b)–(c), respectively. The ADM with airfoil data successfully captures the trends observed in ALM, demonstrating its capability to distribute aerodynamic forces more accurately than traditional uniform-force ADM. In Fig. 6(b), the drag force distribution
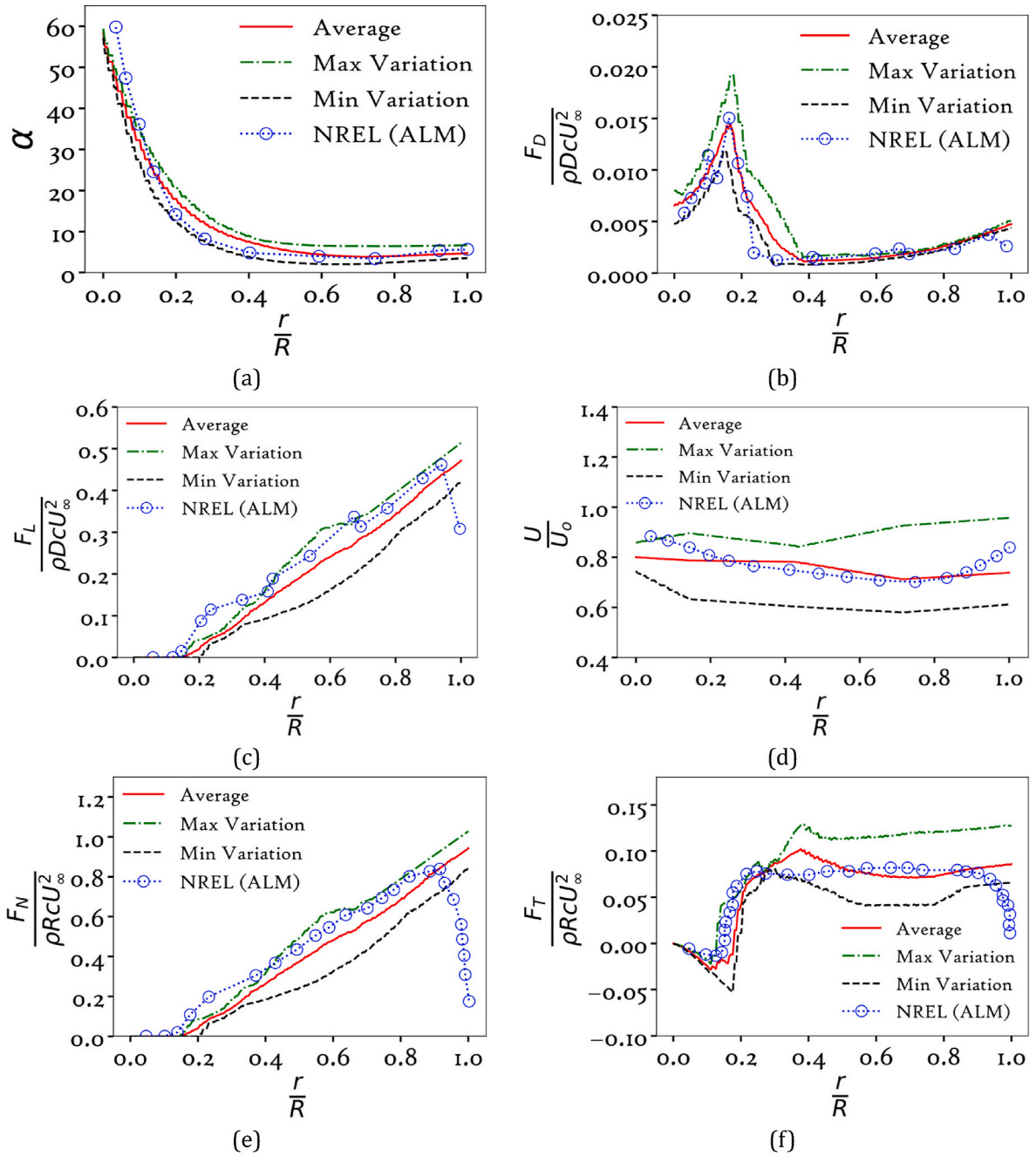
Fig. 6. Results from actuator disk model with airfoil data compared to ALM from literature [29,38,39] (a) angle of attack in degree (b) normalized drag force per unit length (c) normalized lift force per unit length (d) normalized streamwise velocity (e) normalized axial force per unit length and (f) normalized tangential force per unit length. These profiles feature three key representations: the average line, which denotes the mean values across multiple cycles, and the maximum and minimum variation lines, which illustrate the range of fluctuations observed within these cycles. It is noted that this comparison is not perfectly exact due to the differences in the inflow conditions.

shows a peak at approximately $r/R \approx 0.2$, followed by a rapid decay toward the blade tip. The variations in the maximum and minimum values across multiple cycles cover the ALM value from literature. In Fig. 6(c), the lift force distribution follows a monotonic increase from root to tip, as expected. The agreement between ADM and ALM is good, particularly in the region of $r/R < 0.9$. However, as seen with the angle of attack results, ADM shows a mismatch in the trend near the blade tip. This is primarily due to tip effects, which are not explicitly modeled in ADM, leading to an overestimation of loads in this region. The differences in angle of attack seem small in ADM and ALM but the effect amplifies while calculating the lift and drag coefficients. In Fig. 6(d), the normalized velocity is compared against ALM results. The ADM-

predicted velocity field aligns well with ALM, particularly in the central region ($0.20 < r/R < 0.80$). However, the normalized velocity variation along the blade span using ALM always falls in between our maximum and minimum variation lines.

Fig. 6(e) illustrates the normalized normal force distribution along the blade span, comparing results with ALM from the literature. The ADM with airfoil data successfully captures the trends observed in ALM, confirming that ADM captures the aerodynamic loading reasonably well. However, deviations are observed near the blade tip ($r/R > 0.8$), where ADM overestimates the force due to the absence of tip corrections, which was also noted in previous discussions. The maximum and minimum variation in normal force along the span suggests a strong

dependence on transient effects, but the overall agreement with ALM supports the accuracy of ADM with airfoil data in predicting force distribution. Fig. 6(f) represents the normalized tangential force distribution along the blade span. The ADM effectively captures the overall trend observed in ALM. However, a sudden peak is observed in the tangential force near $r/R = 0.4$ which is the artifact of one of the transient load data. Similar to previous findings, the ADM overestimates forces near the tip due to the lack of tip loss corrections, leading to a discrepancy in this region. Despite these differences, the comparison indicates that ADM with airfoil data provides a reasonable approximation of ALM, demonstrating its ability to capture aerodynamic force distributions with high computational efficiency.

The results indicate that the refined ADM with airfoil data significantly improves upon traditional ADM by providing a more realistic force distribution, closely matching ALM predictions. The primary discrepancies arise near the blade tip, where ADM overestimates aerodynamic forces due to the absence of tip loss corrections. Beyond tip correction, there are some other limitations of this airfoil-based actuator disk model. The model extracts all the aerodynamic data along a single line and extends them azimuthally to construct a 3D airfoil-inspired distribution which does not fully capture localized blade features. Therefore, the lift and drag forces distributed in a 3D airfoil introduce approximations in the spatial force distribution. Furthermore, since the implementation is based on local interpolation rather than resolving true blade geometry, secondary flows and tip vortex dynamics are inherently underrepresented. Despite these limitations, the overall agreement between ADM and ALM suggests that the current airfoil-

based refined ADM is a computationally efficient alternative for large-scale wind turbine simulations. Future improvements can involve the incorporation of tip correction factors, which would further enhance the accuracy of load distribution near the tip of the blades. Since the ADM with airfoil data accurately captures the trends in aerodynamic forces, the next step is to utilize these transient load variations at different locations during the blade revolution for structural simulations.

4.2. Transient aerodynamic load variation

In this section, we have analyzed the transient aerodynamic load variations experienced by the wind turbine blade at different instants throughout multiple complete rotational cycles. This section provides insights into how aerodynamic loading evolves as the blade moves through different azimuthal positions. Since we are working on a LES-based ADM framework, the aerodynamic loads fluctuate due to turbulent inflow and wake interactions. For clarity, we have reported only the average loads over a few complete cycles in Fig. 7. However, like the previous analyses, the maximum and minimum variations over these complete cycles are also computed which will be used in the structural simulation in the next section. The maximum and minimum variation lines illustrate the range of fluctuations observed within these cycles. The reported results in Fig. 7 demonstrate how blade position relative to wind direction influences the loading pattern. We assumed that at $t=0$, the blade is at the top of the disk, at $t=T/2$, it rotates to the bottom and at $t=T$, it completes a complete cycle and moves back to the top of the disk. However, the selection of the location of $t=0$ is arbitrary and any
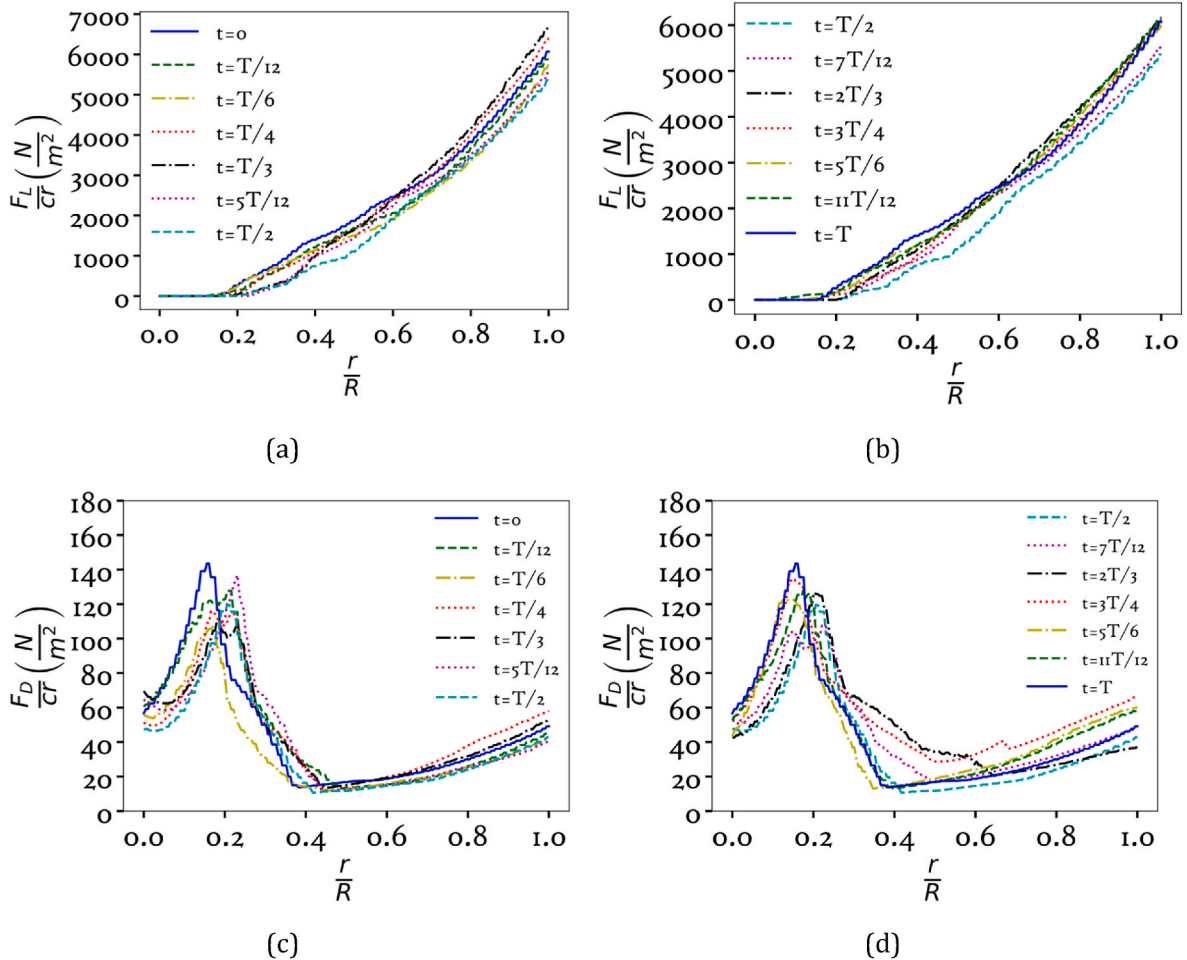

(a)   (b)

(c)   (d)

Fig. 7. Lift and drag force per unit chord and span length at different time of the revolution (a) lift force at first half of revolution (b) lift force at second half of the revolution (c) drag force at first half of the revolution (d) drag force at second half of the revolution.

location on the disk can be selected as the $t=0$ location. In the next section, we will use the average, maximum and minimum cyclic variation of loads in our structural simulations.

Fig. 7 illustrates the evolution of lift and drag per unit chord and span length as a function of the radial position, while different curves represent different instants during the blade's revolution. Each instant of time represents the local position of the blade where variations in wind speed, angle of attack, and relative velocity affect the aerodynamic loading. Fig. 7 (a) and (b) demonstrate that lift force generally follows an increasing trend from the root to the tip of the blade, as expected from conventional blade aerodynamics. Across different time instants, minor fluctuations are observed near the root due to stall effects and lower relative velocity [41]. Unlike the lift force, the drag force exhibits a distinct peak near $r/R \approx 0.2$, which persists across all time instants (Fig. 7(c) and (d)). This peak is associated with the blade section where both induced drag and pressure drag increase significantly.

The aerodynamic loading is critical for understanding wind turbine performance, fatigue life, and structural integrity. Transient variations in aerodynamic forces, such as those observed in our study, directly impact blade bending moments, cyclic fatigue loads, and overall turbine stability. Previous studies, such as Chanprasert et al. [42] and Lanza-fame & Messina [43] have demonstrated that aerodynamic load fluctuations persist even under uniform inflow conditions, emphasizing the role of relative velocity variations and wake interactions. Our findings, which incorporate ABL inflow, further highlight that realistic turbulence conditions can amplify these variations. In the next section, our goal is to use this aerodynamic loading information to calculate the deflection and maximum stress at different instant of time during the revolution of the blade.

4.3. Structural simulation of blade

The lift and drag forces at different instants of time obtained from the previous sections are used in this structural simulation. In our structural simulation, we have only considered the lift and drag force. The gravity effect is not considered in the current study, but we want to add it for future simulations. Similar to prior sections, three loads are employed at a certain time- average load as well as maximum and minimum load variations. In this study, our goal is to obtain the tip deflections, maximum stress and stress concentration location using the transient load variation.

4.3.1. Tip deflections

Tip deflections can lead to blade-tower collisions. There have been significant accidents in which the blades hit the tower in USA and Denmark in 2008, France in 2004 and Germany in 1999 [44,45]. To avoid this blade to tower collisions the maximum variation of the tip

deflection at different locations of the revolution is very important.

Since we have provided transient load information over a few cycles, it is quite difficult to find out a clear trend. Nevertheless, we can see from Fig. 9(a) that from $t=0$ to $t=T/2$, there is a decrease in tip deflection (except $t=T/4$ and $T/3$) and from $t=T/2$ to $t=T$, there is an increase in tip deflections. This pattern of tip deflections is due to the fact that the wind speed is highest at the top location due to the atmospheric boundary layer effect.

From the contour plot in Fig. 8 and flap wise deflection plot in Fig. 9 (b), it is observed that the deflection is nearly 0 near the root and gradually increases near the tip of the blade. Regardless of the loading conditions, the peak deflection occurs at the blade tip and the maximum value of the tip deflection over the complete cycles is found as 4.28m, which is around 6.79 % of the blade length and the minimum value of tip deflection is found as 2.33m, which is around 3.69 % of the blade length.

Shakra et al. [45] found that the maximum deflection value is around 4.3 % of the blade length for NREL wind turbine. They also calculated the flap wise deflection using Blade Element Method (BEM). BEM predicted higher mean blade deflection than CFD. The average flap wise deflection using BEM is around 3.9m which is around 6.34 % of the blade length [45]. Though the inflow and loading conditions are very different, our maximum tip deflection is quite close to their values. For $0°$ yaw angles, Jeong et al. [46] found that deflection is around 4.5m which is around 7.14 % of the blade length. Dose et al. [47] found that the flap wise deflection is around 6m which is around 9.75 % of the blade length. After comparing with the previous literature, we can say that our result is reasonably close to the reported values in the literature though the flow and loading conditions are different. We also calculated the edgewise deflection and found that edgewise deflections are very small compared to the flap wise deflection which is also consistent with the prior studies [45].

4.3.2. Maximum stress and stress concentration

The structural response of wind turbine blades under transient aerodynamic loading is crucial for assessing fatigue life, material performance, and potential failure risks [41,48]. In the present analysis, our focus is to study stress distribution and the regions where maximum stress and stress concentration occur due to aerodynamic loads and blade flexibility. We have employed Von-Mises stress to determine the maximum stresses and stress concentration location, which is calculated as [49,50]:

$$\sigma_v = \sqrt{\frac{1}{2}\left[(\sigma_1 - \sigma_2)^2 + (\sigma_2 - \sigma_3)^2 + (\sigma_3 - \sigma_1)^2 \right]} \qquad (11)$$

where σ_v denotes the Von-Mises stress; σ_1, σ_2 and σ_3 are the principal stresses in the stress space, respectively. In future work, we will focus on
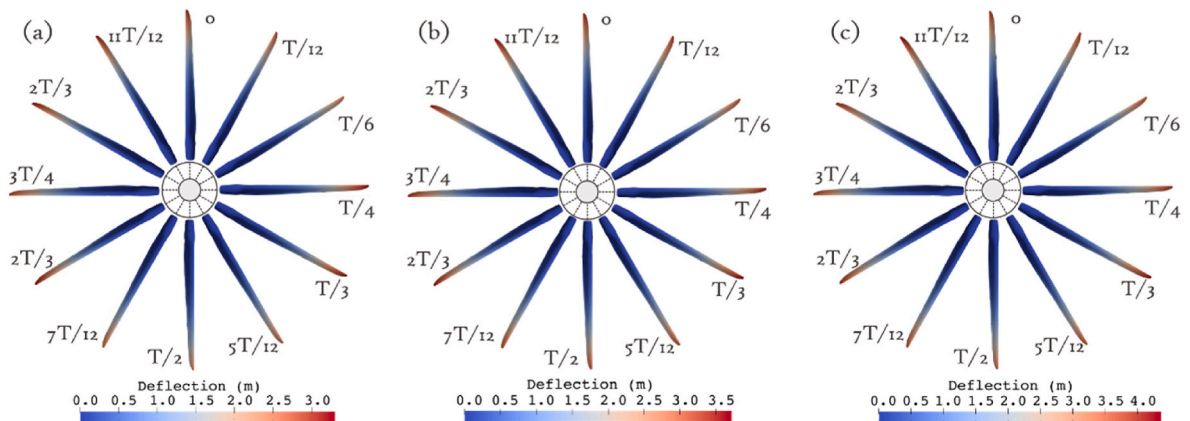

Fig. 8. Flap wise deflection at different instances of revolution using (a) minimum cyclic variation of lift and drag force (b) average lift and drag force and (c) maximum cyclic variation of lift and drag force.
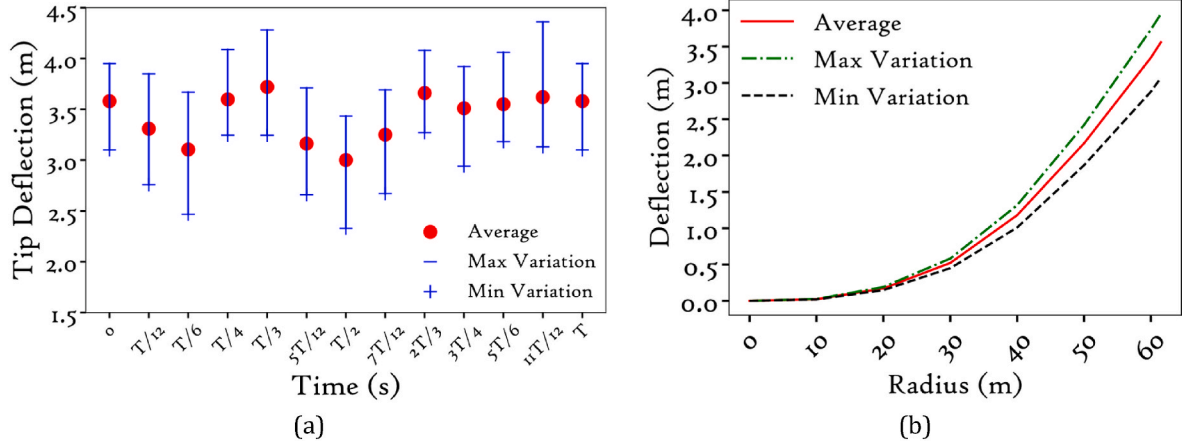
Fig. 9. (a) Tip deflection at different instances of revolution (b) flap wise deflection along the radius at t = 0 location over multiple cycles.

fatigue life, buckling and material performance.

From Figs. 10 and 12, it is evident that the maximum stress concentration occurs near the root of the blade ($r/R \approx 0.2$). There are two other locations where higher stress might occur-at the root of the blade and the mid span of the blade. At the root region, significant stress occurs due to the rigid attachment to the hub, where high bending moments are transmitted from the rotating blade to the turbine structure. This region is typically reinforced with thicker composite laminates to withstand high stress, reducing the risk of material failure. The region near the root of the blade experiences the highest localized stress concentration, as seen in Fig. 12. The highest localized stress concentration over the cycles is reported in Fig. 11. As shown in Fig. 11, the maximum stress exhibits a decreasing trend from $t = 0$ to $t = T/2$ (except $t = T/4$ and T/3), and then increases from $t = T/2$ to $t = T$. Similar to the analysis of tip deflection in Fig. 9(a), such a variation of maximum stress arises from the fact that wind speed reaches its peak at the top location induced by the atmospheric boundary layer effect [51,52].

This peak of stress results from the transition in structural stiffness from the root to the flexible blade sections, combined with high aerodynamic loading and bending moments. The results suggest that this location is a critical point for stress accumulation, making it an ideal target for structural reinforcements. At the blade mid span region, the stress levels are generally lower than the near root regions. Near the tip of the blade, minimum stress is found. However, deflections are higher in this region due to aerodynamic forces and blade flexibility. Previous studies support our findings on stress distribution and maximum stress concentration location. Shen et al. [48] showed that dynamic stall
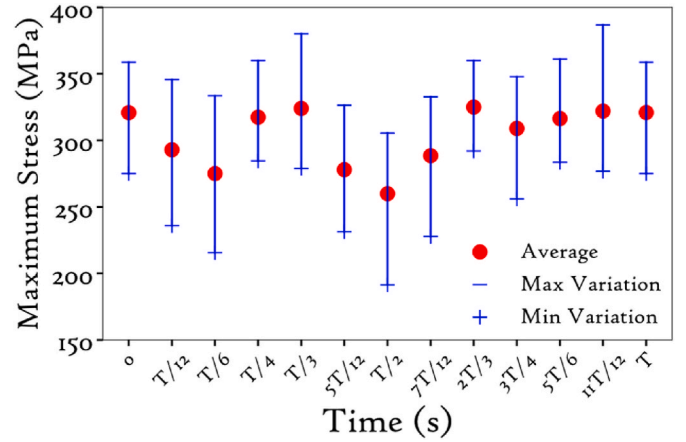

Fig. 11. Maximum stress along the blade at different instances of revolution.

effects significantly influence stress distribution, particularly at the root and near root regions. This finding is consistent with our observation that high stress fluctuations occur near $r/R \approx 0.2$, making it a crucial area for structural optimization. The root region endures significant bending moments, while the blade tip undergoes large deflections.
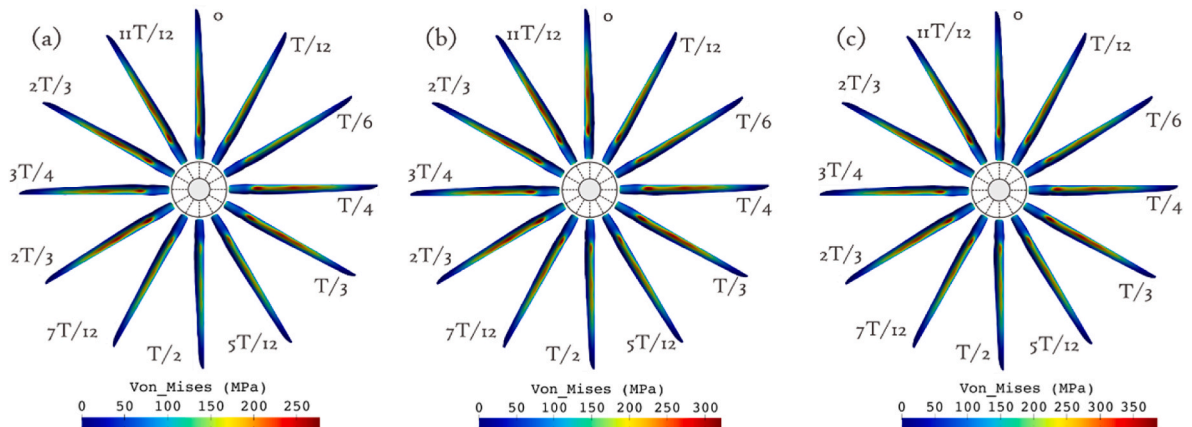

Fig. 10. Stress distribution along the blade at different instances of revolution- (a) minimum variation over multiple cycles (b) average variation over multiple cycles and (c) maximum variation over multiple cycles.
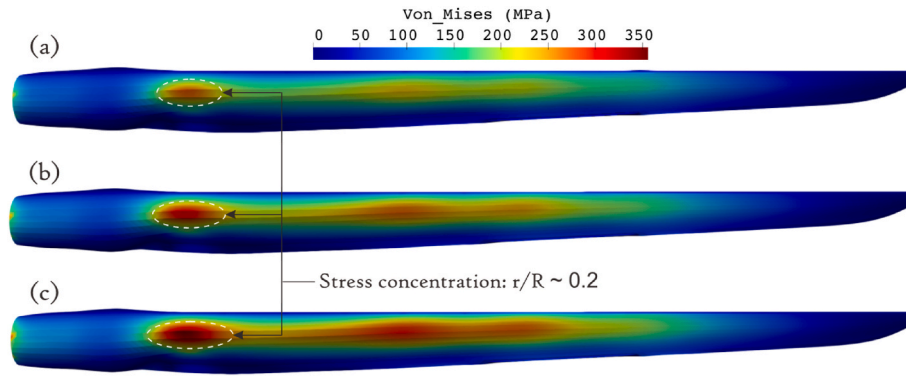
Fig. 12. Stress concentration at $t = 0$ location of the revolution using (a) minimum lift and drag force distribution (b) average lift and drag force distribution and (c) maximum lift and drag force distribution. For all these cases, the location of maximum stress concentration is near the root of the blade ($r/R \approx 0.2$).

5. Limitations and future works

Despite the improvements introduced by our airfoil-based actuator disk model, there remain several limitations. The model extracts aerodynamic data along a single line and extends them azimuthally, lacking true spanwise resolution. Moreover, the interpolation-based force implementation does not fully capture secondary flows or tip vortex dynamics that play a key role in wake behavior and downstream turbulence. Additionally, the present model does not incorporate tip-loss corrections, Coriolis forces, and gravitational effects. Our airfoil-based ADM overestimates the aerodynamic force near the tip due to the absence of tip loss corrections. Tip-losses play a significant role in reducing effective circulation near the blade ends, which directly influences both thrust and structural loading distribution. Furthermore, the lack of tip-loss correction may slightly reduce the overall accuracy in the full-scale wind farm applications. In full-scale settings, inaccuracies in the outer rotor region can influence wake development and downstream turbine performance.

In our future work, by incorporating a robust tip-loss correction, we aim to make our airfoil-based ADM more suitable for scalable high-fidelity simulations where computational efficiency will be more balanced with physical accuracy. While classical tip-loss correction methods exist, they often rely on empirical assumptions. Therefore, we are planning to explore more advanced force distribution strategies that can better capture these effects without relying heavily on the empirical corrections. This correction will be included in the calculation of local lift (F_L) and drag (F_D) forces per unit area which will allow the model to better represent the variation of aerodynamic load distribution [38,39]. We are also planning to incorporate Coriolis forces and gravitational effects, investigate blade-tower interaction, and conduct fatigue and buckling analysis for the full-scale wind farm.

6. Concluding remarks

This study introduces an enhanced Actuator Disk Model incorporating airfoil data and interpolation-based refinement to balance computational efficiency with improved accuracy for wind turbine aerodynamic and structural analysis. Our approach bridges the gap between traditional ADM and more intensive Actuator Line Model techniques, significantly enhancing spatial resolution through grid refinement while maintaining computational efficiency.

Comparative analysis with ALM shows strong agreement in predicting key aerodynamic parameters like angle of attack, axial velocity, lift, drag, axial and tangential forces across most of the blade span (r/R < 0.90), with some discrepancies near the tip due to the absence of tip correction factors. This limitation leads to an overestimation of aerodynamic forces in the tip region. However, the overall agreement between ADM and ALM suggests that our airfoil-based ADM provides a computationally efficient alternative that captures the essential aerodynamic characteristics required for structural simulations.

A strategic enhancement of our approach is its ability to track transient aerodynamic load variations over multiple cycles. Unlike the conventional Actuator Disk Model, which typically provides only time-averaged forces, our method captures transient variations in aerodynamic loading. This enables finding out the maximum and minimum load variations at any particular location of the blade during revolution across different cycles, which is critical for accurate structural analysis, particularly for assessing potential failure risks in wind turbine blades.

The transient aerodynamic load analysis reveals significant variations throughout different cycles, influenced by the local flow conditions and the atmospheric boundary layer. Our results show that the lift force generally follows an increasing trend from the root to the tip of the blade, while the drag force exhibits a distinct peak near $r/R \approx 0.2$, persisting across all time instants. Structural simulations revealed maximum tip deflection of 4.28 m (6.79 % of blade length), with stress concentrations occurring primarily near the blade root ($r/R \approx 0.2$), aligning with previous studies [45,46,48]. These findings provide valuable guidance for structural optimization in blade design.

Despite its advantages, our approach has several limitations. The model extracts aerodynamic data along a single line and extends them azimuthally, lacking true spanwise resolution. The distribution of lift and drag forces in the 3D airfoil introduces spatial approximations, and the interpolation-based implementation underrepresents any secondary flows and tip vortex dynamics. Additionally, the current model does not account for the tip correction factors, Coriolis forces, and gravitational effects. Future work will address these limitations by implementing correction factors, incorporating gravitational effects, investigating blade-tower interaction, and conducting fatigue and buckling analysis for the full-scale wind farm.

In conclusion, this study introduces an airfoil-based actuator disk model with interpolation-based grid refinement, offering a practical balance between accuracy and computational efficiency. By capturing both time-averaged and transient aerodynamic loads, the approach enables improved blade performance analysis without the expense of fully resolved models. This method can accelerate wind turbine design and optimization, contributing to more reliable and cost-effective wind energy systems.

CRediT authorship contribution statement

Muhammad Rubayat Bin Shahadat: Writing – review & editing, Writing – original draft, Visualization, Validation, Software, Methodology, Investigation, Formal analysis, Data curation, Conceptualization. **Mohammad Hossein Doranehgard:** Writing – review & editing, Writing – original draft, Visualization, Validation, Software, Methodology, Investigation, Formal analysis, Data curation, Conceptualization.

Weibing Cai: Writing – original draft, Visualization, Software, Methodology, Data curation, Conceptualization. **Charles Meneveau:** Writing – review & editing, Writing – original draft, Validation, Supervision, Software, Resources, Project administration, Methodology, Investigation, Funding acquisition, Formal analysis, Conceptualization. **Benjamin Schafer:** Writing – review & editing, Writing – original draft, Validation, Supervision, Software, Resources, Project administration, Methodology, Investigation, Funding acquisition, Formal analysis, Conceptualization. **Zheng Li:** Writing – review & editing, Writing – original draft, Visualization, Validation, Software, Resources, Project administration, Methodology, Investigation, Funding acquisition, Formal analysis, Data curation, Conceptualization.

Declaration of competing interest

The authors declare that they have no known competing financial interests or personal relationships that could have appeared to influence the work reported in this paper.

Acknowledgement

References

[1] M. Eichhorn, P. Tafarte, D. Thrän, Towards energy landscapes – "pathfinder for sustainable wind power locations.", Energy 134 (2017) 611–621, https://doi.org/10.1016/j.energy.2017.05.053.

[2] M. Shields, P. Beiter, J. Nunemaker, A. Cooperman, P. Duffy, Impacts of turbine and plant upsizing on the levelized cost of energy for offshore wind, Appl. Energy 298 (2021) 117189, https://doi.org/10.1016/j.apenergy.2021.117189.

[3] J.F. DeCarolis, D.W. Keith, The economics of large-scale wind power in a carbon constrained world, Energy Policy 34 (2006) 395–410, https://doi.org/10.1016/j.enpol.2004.06.007.

[4] L. Kosharska, V. Brednyova, Nikiforov Yu, Green Energy: a Modern View in Conditions of Environmental Safety, Her Odessa Natl Marit Univ, 2024, pp. 225–233, https://doi.org/10.47049/2226-1893-2024-2-225-233.

[5] M. Ortega, P.D. Río, P. Ruiz, C. Thiel, Employment effects of renewable electricity deployment. A novel methodology, Energy 91 (2015) 940–951, https://doi.org/10.1016/j.energy.2015.08.061.

[6] S.S. Tomar, A. Dewan, Investigating wake characteristics of savonius turbine for off-grid wind energy: analyzing operating influences, Energy 316 (2025) 134563, https://doi.org/10.1016/j.energy.2025.134563.

[7] R. Bontempo, E.M. Di Marzo, M. Manna, Coupled and uncoupled CFD-Based design strategies for diffuser-augmented wind turbines: a comparative study, Energy 314 (2025) 134159, https://doi.org/10.1016/j.energy.2024.134159.

[8] X. Yang, M. Pakula, F. Sotiropoulos, Large-eddy simulation of a utility-scale wind farm in complex terrain, Appl. Energy 229 (2018) 767–777, https://doi.org/10.1016/j.apenergy.2018.08.049.

[9] H. Zhong, P. Du, F. Tang, L. Wang, Lagrangian dynamic large-eddy simulation of wind turbine near wakes combined with an actuator line method, Appl. Energy 144 (2015) 224–233, https://doi.org/10.1016/j.apenergy.2015.01.082.

[10] S. Amini, M.R. Golzarian, E. Mahmoodi, A. Jeromin, M.H. Abbaspour-Fard, Numerical simulation of the Mexico wind turbine using the actuator disk model along with the 3D correction of aerodynamic coefficients in OpenFOAM, Renew. Energy 163 (2021) 2029–2036, https://doi.org/10.1016/j.renene.2020.10.120.

[11] A. Behrouzifar, M. Darbandi, Developing the actuator disk model to predict the fluid–structure interaction in numerical simulation of multimegawatt wind turbine blades, J. Energy Resour. Technol. 142 (2020) 031204, https://doi.org/10.1115/1.4044576.

[12] V. Chabaud, Rotor-integrated modeling of wind turbine aerodynamics, Wind Energy 24 (2021) 1199–1224, https://doi.org/10.1002/we.2626.

[13] L.A. Martínez-Tossas, M.J. Churchfield, S. Leonardi, Large eddy simulations of the flow past wind turbines: actuator line and disk modeling: LES of the flow past wind turbines: actuator line and disk modeling, Wind Energy 18 (2015) 1047–1060, https://doi.org/10.1002/we.1747.

[14] E.L. Hodgson, C. Grinderslev, A.R. Meyer Forsting, N. Troldborg, N.N. Sørensen, J. N. Sørensen, et al., Validation of aeroelastic actuator line for wind turbine modelling in complex flows, Front. Energy Res. 10 (2022) 864645, https://doi.org/10.3389/fenrg.2022.864645.

[15] L. Cacciali, M.O.L. Hansen, K. Rogowski, Highly stable lattice boltzmann method with a 2-D actuator line model for vertical axis wind turbines, Energies 17 (2024) 4847, https://doi.org/10.3390/en17194847.

[16] C. Muyan, D. Coker, Finite element simulations for investigating the strength characteristics of a 5 m composite wind turbine blade, Wind Energy Sci 5 (2020) 1339–1358, https://doi.org/10.5194/wes-5-1339-2020.

[17] I. Alrowwad, X. Wang, N. Zhou, Numerical modelling and simulation analysis of wind blades: a critical review, Clean Energy 8 (2024) 261–279, https://doi.org/10.1093/ce/zkad078.

[18] Larsen TJ, Box PO. Aeroelastic Effects of Large Blade Deflections for Wind Turbines n.d.

[19] H.M.S.M. Mazarbhuiya, A. Biswas, K.K. Sharma, Blade thickness effect on the aerodynamic performance of an asymmetric NACA six series blade vertical axis wind turbine in low wind speed, Int. J. Green Energy 17 (2020) 171–179, https://doi.org/10.1080/15435075.2020.1712214.

[20] O. Rajad, H. Mounir, A.E. Marjani, Fertahi S. ed-Dîn, Nonlinear modeling analysis of the coupled mechanical strength and stiffness enhancement of composite materials of a horizontal axis wind turbine blade (HAWTB), Int J Interact Des Manuf IJIDeM 16 (2022) 469–492, https://doi.org/10.1007/s12008-021-00790-0.

[21] H. Li, W. Ning, W. Xin, B. Xu, Study on the delamination damage prediction of wind turbine blade spar cap based on morphology feature recognition, Eng. Fail. Anal. 166 (2024) 108867, https://doi.org/10.1016/j.engfailanal.2024.108867.

[22] X. Chen, X. Zhao, J. Xu, Revisiting the structural collapse of a 52.3 m composite wind turbine blade in a full-scale bending test, Wind Energy 20 (2017) 1111–1127, https://doi.org/10.1002/we.2087.

[23] P.U. Haselbach, An advanced structural trailing edge modelling method for wind turbine blades, Compos. Struct. 180 (2017) 521–530, https://doi.org/10.1016/j.compstruct.2017.08.029.

[24] E. Bou-Zeid, C. Meneveau, M. Parlange, A scale-dependent Lagrangian dynamic model for large eddy simulation of complex turbulent flows, Phys. Fluids 17 (2005) 025105, https://doi.org/10.1063/1.1839152.

[25] C. VerHulst, C. Meneveau, Large eddy simulation study of the kinetic energy entrainment by energetic turbulent flow structures in large wind farms, Phys. Fluids 26 (2014) 025113, https://doi.org/10.1063/1.4865755.

[26] M. Calaf, C. Meneveau, J. Meyers, Large eddy simulation study of fully developed wind-turbine array boundary layers, Phys. Fluids 22 (2010) 015110, https://doi.org/10.1063/1.3291077.

[27] R.J.A.M. Stevens, D.F. Gayme, C. Meneveau, Large eddy simulation studies of the effects of alignment and wind farm length, J. Renew. Sustain. Energy 6 (2014) 023105, https://doi.org/10.1063/1.4869568.

[28] C. VerHulst, C. Meneveau, Altering kinetic energy entrainment in large eddy simulations of large wind farms using unconventional wind turbine actuator forcing, Energies 8 (2015) 370–386, https://doi.org/10.3390/en8010370.

[29] L.A. Martínez-Tossas, M.J. Churchfield, C. Meneveau, Large eddy simulation of wind turbine wakes: detailed comparisons of two codes focusing on effects of numerics and subgrid modeling, J Phys Conf Ser 625 (2015) 012024, https://doi.org/10.1088/1742-6596/625/1/012024.

[30] M.R. Bin Shahadat, M.H. Doranehgard, W. Cai, Z. Li, Large eddy simulation of wind farm performance in horizontally and vertically staggered layouts, Energy 322 (2025) 135569, https://doi.org/10.1016/j.energy.2025.135569.

[31] L. Martinez, S. Leonardi, M. Churchfield, P. Moriarty, A comparison of actuator disk and actuator line wind turbine models and best practices for their use. 50th AIAA Aerosp. Sci. Meet. New Horiz. Forum Aerosp. Expo., Nashville, Tennessee, American Institute of Aeronautics and Astronautics, 2012, https://doi.org/10.2514/6.2012-900.

[32] F. Porté-Agel, M. Bastankhah, S. Shamsoddin, Wind-turbine and wind-farm flows: a review, Bound-Layer Meteorol 174 (2020) 1–59, https://doi.org/10.1007/s10546-019-00473-0.

[33] J. Jonkman, S. Butterfield, W. Musial, G. Scott, Definition of a 5-MW reference wind turbine for offshore system development. https://doi.org/10.2172/947422, 2009.

[34] M.-K. Yeh, C.-H. Wang, Stress analysis of composite wind turbine blade with different stacking angle and different skin thickness, DEStech Trans Mater Sci Eng (2017), https://doi.org/10.12783/dtmse/icmsea/mce2017/10875.

[35] W.A. Timmer, R.P.J.O.M. Van Rooij, Summary of the delft university wind turbine dedicated airfoils, J. Sol. Energy Eng. 125 (2003) 488–496, https://doi.org/10.1115/1.1626129.

[36] K. Cox, A. Echtermeyer, Structural design and analysis of a 10MW wind turbine blade, Energy Proc. 24 (2012) 194–201, https://doi.org/10.1016/j.egypro.2012.06.101.

[37] A. Algolfat, Weizhuo Wang, Alhussein Albarbar, Dynamic responses analysis of A 5MW NREL wind turbine blade under flap-wise and edge-wise vibrations, J Dyn Monit Diagn (2022) 208–222, https://doi.org/10.37965/jdmd.2022.108.

[38] Diaz GP. Navarro, A.D. Otero, H. Asmuth, J.N. Sørensen, S. Ivanell, Actuator line model using simplified force calculation methods, Wind Energy Sci 8 (2023) 363–382, https://doi.org/10.5194/wes-8-363-2023.

[39] P. Réthoré, P. Van Der Laan, N. Troldborg, F. Zahle, N.N. Sørensen, Verification and validation of an actuator disc model, Wind Energy 17 (2014) 919–937, https://doi.org/10.1002/we.1607.

[40] Y.-T. Wu, F. Porté-Agel, Large-eddy simulation of wind-turbine wakes: evaluation of turbine parametrisations, Bound-Layer Meteorol 138 (2011) 345–366, https://doi.org/10.1007/s10546-010-9569-x.

[41] D.M. Elsherif, A.A. Abd El-Wahab, M.H. Abdellatif, Factors affecting stress distribution in wind turbine blade, IOP Conf. Ser. Mater. Sci. Eng. 610 (2019) 012020, https://doi.org/10.1088/1757-899X/610/1/012020.

[42] W. Chanprasert, R.N. Sharma, J.E. Cater, S.E. Norris, Large eddy simulation of wind turbine fatigue loading and yaw dynamics induced by wake turbulence, Renew. Energy 190 (2022) 208–222, https://doi.org/10.1016/j.renene.2022.03.097.

[43] R. Lanzafame, M. Messina, Horizontal axis wind turbine working at maximum power coefficient continuously, Renew. Energy 35 (2010) 301–306, https://doi.org/10.1016/j.renene.2009.06.020.

[44] M. Zhao, W. Yu, P. Wang, Y. Qu, X. Du, Numerical study on the aerodynamic and fluid–structure interaction of an NREL-5MW wind turbine, China Ocean Eng. 38 (2024) 363–378, https://doi.org/10.1007/s13344-024-0030-1.

[45] Y. Shkara, M. Cardaun, R. Schelenz, G. Jacobs, Aeroelastic response of a multi-megawatt upwind horizontal axis wind turbine (HAWT) based on fluid–structure interaction simulation, Wind Energy Sci 5 (2020) 141–154, https://doi.org/10.5194/wes-5-141-2020.

[46] M.-S. Jeong, S.-W. Kim, I. Lee, S.-J. Yoo, K.C. Park, The impact of yaw error on aeroelastic characteristics of a horizontal axis wind turbine blade, Renew. Energy 60 (2013) 256–268, https://doi.org/10.1016/j.renene.2013.05.014.

[47] B. Dose, H. Rahimi, I. Herráez, B. Stoevesandt, J. Peinke, Fluid-structure coupled computations of the NREL 5MW wind turbine blade during standstill, J Phys Conf Ser 753 (2016) 022034, https://doi.org/10.1088/1742-6596/753/2/022034.

[48] W.Z. Shen, M.O.L. Hansen, J.N. Sørensen, Determination of the angle of attack on rotor blades, Wind Energy 12 (2009) 91–98, https://doi.org/10.1002/we.277.

[49] B. Gallien, M. Albaric, T. Duffar, K. Kakimoto, M. M'Hamdi, Study on the usage of a commercial software (Comsol-Multiphysics®) for dislocation multiplication model, J. Cryst. Growth 457 (2017) 60–64, https://doi.org/10.1016/j.jcrysgro.2016.05.027.

[50] * W.M. Huang, X.Y. Gao, Tresca and von Mises yield criteria: a view from strain space, Philos. Mag. Lett. 84 (2004) 625–629, https://doi.org/10.1080/09500830512331325091.

[51] R.G.J. Flay, D.C. Stevenson, D. Lindley, Wind structure in a rural atmospheric boundary layer near the ground, J. Wind Eng. Ind. Aerod. 10 (1982) 63–78, https://doi.org/10.1016/0167-6105(82)90054-X.

[52] B. Yang, L.K. Berg, Y. Qian, C. Wang, Z. Hou, Y. Liu, et al., Parametric and structural sensitivities of turbine-height wind speeds in the boundary layer parameterizations in the weather research and forecasting model, J Geophys Res Atmospheres 124 (2019) 5951–5969, https://doi.org/10.1029/2018JD029691.